applied sciences

MDPI

Article

Low-Cost $CuIn_{1-x}Ga_xSe_2$ Ultra-Thin Hole-Transporting Material Layer for Perovskite/CIGSe Heterojunction Solar Cells

Liann-Be Chang [1], Chzu-Chiang Tseng [1], Gwomei Wu [1,*], Wu-Shiung Feng [1], Ming-Jer Jeng [1], Lung-Chien Chen [2], Kuan-Lin Lee [2], Ewa Popko [3], Lucjan Jacak [3] and Katarzyna Gwozdz [3]

1 Institute of Electro-Optical Engineering, Green Technology Research Center, Department of Electronic Engineering, Chang Gung University, Chang Gung Memorial Hospital, Taoyuan 333, Taiwan; liann@mail.cgu.edu.tw (L.-B.C.); D0427101@cgu.edu.tw (C.-C.T.); ws.feng@msa.hinet.net (W.-S.F.); mjjeng@mail.cgu.edu.tw (M.-J.J.)

2 Department of Electro-Optical Engineering, National Taipei University of Technology, Taipei 106, Taiwan; ocean@ntut.edu.tw (L.-C.C.); t102658016@gmail.com (K.-L.L.)

3 Department of Quantum Technologies, Wroclaw University of Science Technology, Wroclaw 50-370, Poland; Ewa.Popko@pwr.edu.pl (E.P.); Lucjan.Jacak@pwr.edu.pl (L.J.); katarzyna.r.gwozdz@pwr.edu.pl (K.G.)

* Correspondence: wu@mail.cgu.edu.tw; Tel.: +886-3-211-8800

Received: 17 December 2018; Accepted: 15 February 2019; Published: 19 February 2019

Abstract: This paper presents a new type of solar cellwith enhanced optical-current characteristics using an ultra-thin $CuIn_{1-x}Ga_xSe_2$ hole-transporting material (HTM) layer (<400 nm). The HTM layer was between a bi-layer Mo metal-electrode and a $CH_3NH_3PbI_3$ ($MAPbI_3$) perovskite active absorbing material. It promoted carrier transportand led to an improved device with good ohmic-contacts. The solar cell was prepared as a bi-layer Mo/$CuIn_{1-x}Ga_xSe_2$/perovskite/C_{60}/Ag multilayer of nano-structures on an FTO (fluorine-doped tin oxide) glass substrate. The ultra-thin $CuIn_{1-x}Ga_xSe_2$ HTM layers were annealed at various temperatures of 400, 500, and 600 °C. Scanning electron microscopy studies revealed that the nano-crystal grain size of $CuIn_{1-x}Ga_xSe_2$ increased with the annealing temperature. The solar cell results show an improved optical power conversion efficiency at ~14.2%. The application of the $CuIn_{1-x}Ga_xSe_2$ layer with the perovskite absorbing material could be used for designing solar cells with a reduced HTM thickness. The $CuIn_{1-x}Ga_xSe_2$ HTM has been evidenced to maintain a properopen circuit voltage, short-circuit current density and photovoltaic stability.

Keywords: CIGSe; hole-transporting material (HTM); perovskite; $MoSe_2$; C_{60}

1. Introduction

Hybrid organic-inorganic perovskite materials exhibit the advantages of easy fabrication, a large absorption coefficient, an adjustable energy band gap, high carrier mobility, and a long charge carrier diffusion length [1–4]. Metal halide-based perovskite solar cells (PSCs) have aimed for a better power conversion efficiency (PCE) for the next generationof photovoltaics [5–7].It should be pointed out that even if a lot of effort has been spent on the development of novel alternative solar cells like quantum dot solar cells [8] and single-material organic solar cells [9], perovskite-like solar cells are the most promising type of photovoltaic devices. To comprehend the green renewable energy demand, not only the cost-effectiveness of photovoltaic systems but also the expansion of its installation locations should be carefully established. Since the utility market facility has to regulate its growth rate, building-integrated photovoltaics is a potential candidate to solve such green renewable energy expectation.

In recent years, organic-inorganic hybrid substances, the remarkably dictated perovskite family, has shown great distinction for field-effect solar cells [10,11]. Lately, the PCE of lead halide perovskite ($CH_3NH_3PbX_3$, X = Cl, Br, I)–based thin-film photovoltaic devices reached 22% [12–16]. The organic metal halide material has excellent performance for solarphoton harvesting due to its low energy band gap and large excitation diffusion length [17,18]. The optical energy band gap of organic metal perovskite ($CH_3NH_3PbI_3$; $MAPbI_3$) is ~1.56 eV. Consequently, this material benefits from efficient carrier generation and transportation to electrodes that can harvest sunlight radiation fromthe ultra-violet to infrared region. The diffusion length is more than one micrometer in the mixed halide perovskite [18]. Miyasaka et al. have investigated an organometal halide perovskite solar cell with a mesoporous TiO_2. They used a $CH_3NH_3PbI_3$ and $CH_3NH_3PbBr_3$ nano-crystal material as absorbers, achieving an efficiency of 3.8% [19]. In 2012, Park and Gratzel et al. researched a complete solid-state perovskite solar cell withan FTO (fluorine-tin-oxide)/mesoporous TiO_2/perovskite/2,2′,7,7′-tetrakis(N,N-di-p-methoxyphenyl-amino),9,9′spirobifluorene(SpiroOMeTAD)/gold structure, achieving an efficiency of 9% [20]. One year later, the first unique inverted planar composition nano-structure of a perovskite solar cell was announced and a similar nano-structure device was used in other organic perovskite solar cells [21]. This inverted nano-structure was fabricated on ITO (indium-tin-oxide)/poly(3,4-ethylene-dioxythiophene):poly(styrene-sulfonate) (PEDOT:PSS)/perovskite/(6,6)phenyl-C61-butyric-acid-methylester(PCBM)/silver, and PEDOT:PSS was used as the hole-transporting material(HTM). However, the traditional hole-transporting material of PEDOT:PSS is acidic, which can erode ITO and decrease the reliability of the perovskite solar cells [22,23]. Further investigations into the efficiency are still required for solar cells using other thin film materials, such as CdTe and $CuIn_{1-x}Ga_xSe_2$ [24].

Lately, Christians et al. evaluateda film interface-related reducing mechanism and improved the PCE stability of small-area solar cells [25]. Photovoltaic technology has showncontinuous improvement, withenhanced device stability and improved cell durability. The future prospects areindeed obvious for the renewable energy realm [26]. The stability requirements can be established by solar cell devices with a unique combination of material composition and device structure, toward cell efficiency, scalability, and durability [27]. Usually, FTO is used to replace ITO asthe transparent conducting oxide (TCO). The TCO is deposited on top of a glass substrate, such as in dye-sensitized solar cells and perovskite-based solar cells. The ITO electrical conductivity can be reduced in the presenceof oxygen at a relatively high temperature, such as around 500 °C. However, FTO is much more stable under a heat annealing environment. In addition, FTO has been distinguished for its use in numerous multi-structure photovoltaics and nano-structured devices [28,29].

Moreover, few investigators have studied metal-selenide as a carrier-transporting material for perovskite photovoltaic devices [30,31]. The metal-selenide material has attracted significant attention due to its outstanding optical properties and electric characteristics. Moreover, the energy band gap can be adjusted between 1.0 and 1.7 eV by varying the In:Ga ratio [32]. This also provides the possibility for tandem solar cells. The traditional standard thickness of $CuIn_{1-x}Ga_xSe_2$ absorber layer has been about 2–3 μm [33–35]. It is desirable to thin down the absorber layer's thickness to below 1 μm. This would improve recombination at the back contact layer [36,37]. The recombination can be decreased by changing the In:Ga ratio toward the back contact layer, directing to a beneficial electron reaction and reducing the active absorber layer thickness to essentially decrease light absorption. Nevertheless, light trapping in $CuIn_{1-x}Ga_xSe_2$ ultra-thin solar cellsfaces challenges in crystallization growth and parasitic photon absorption at the Mo back metal-electrode contact layer. The absorption loss at the back contact layer should be considered for $CuIn_{1-x}Ga_xSe_2$ solar cell before its application in advanced photovoltaic devices [38,39].

Even now, $CuIn_{1-x}Ga_xSe_2$ thin-films are one of the most promising materials for photovoltaic devices because of their high solar photon absorption coefficient and direct energy band gap. They also exhibit a high conversion efficiency on various flexible substrates [39,40]. A small contact resistance between the metallic film and the optical absorber film is inevitable, as the contact resistance adds

toa serial resistance. The Schottky barrier has been reported with a height of approximately 0.8 eV for the p-doped $CuInSe_2$ (011)/Mo metal-contact film [41]. The molybdenum-diselenide ($MoSe_2$) film has significant effects on the behavior of the Mo/$CuIn_{1-x}Ga_xSe_2$ layer interface [42,43]. Mo-O and Mo-O-Se compounds were discovered while being selenized with a Mo film deposited on the substrate with a CuInS film [44]. For a substrate temperature higher than 550 °C, the $MoSe_2$ film thickness increased witha higher annealing temperature [45]. The nano-crystal film orientation and growth rate of the $MoSe_2$ film was dependent upon the selenization temperature. It has been indicated that the construction of a $MoSe_2$ film at the Mo/$CuIn_{1-x}Ga_xSe_2$ layer interface during a three-stage process using the annealing procedure [46]. However, the $MoSe_2$ film did not form under copper-rich conditions, and the characteristics of the $MoSe_2$ film relied on the $CuIn_{1-x}Ga_xSe_2$ deposition technique and the annealing conditions [47,48].

In the past years, researchers have studied the contribution of nano-materials to the efficiency of ultra-thin $CuIn_{1-x}Ga_xSe_2$ solar cells; that would lead to even thinner and more cost-effective devices [49,50]. In addition, a highly defective $CuIn_{1-x}Ga_xSe_2$/TCO interface could affect the connection to the depletion region in a thinned $CuIn_{1-x}Ga_xSe_2$ solar cell, resulting in a high recombination rate between the absorber layer and the back contact layer [51,52]. This recombination and reformation phenomenon is more pronounced in ultra-thin $CuIn_{1-x}Ga_xSe_2$ solar cells. The ultra-thin $CuIn_{1-x}Ga_xSe_2$ HTM structures could be fabricated for the advancement of innovative concepts to increase the CIGSe-based device's performance. It could alsoreducesolar cell device cost, andmaintain perovskite absorber layer's open circuit voltage (V_{oc}), short-circuit current density (J_{SC}), fill factor (FF), and stability [53]. Furthermore, severalHTM materials require lithium salt doping to enhance hole mobility and performance. However, the hygroscopic nature of lithium bis(trifluoromethylsulfonyl)imide (Li-TFSI) could cause a perovskite device todecompose, resulting in problems in stability. Therefore, a few investigators have developed other HTMs witha low cost and high stability for photovoltaic devices [54–56]. In comparison with other organic HTMs, p-type inorganic HTMs have already been studied due to their long-term stability and lower cost [57–60]. It has been encouraging to investigate Cu-based inorganic HTMs with good characteristics, and thus ultra-thin $CuIn_{1-x}Ga_xSe_2$ can act as a new hole-transporting material in solar cells. The Cu-based chalcopyrite semiconductors, such as $CuInS_2$, $CuInSe_2$, $CuIn_{1-x}Ga_xS_2$ (CIGS), $CuIn_{1-x}Ga_xSe_2$ (CIGSe) and CIGSSe, are prospective light-absorbing materials. Recently, $CuInS_2$ and $CuInSe_2$ quantum dots were used as inorganic HTMs to replace the organic hole-transporting spiro-OMeTAD [61]. The relatively low PCE of Cu-based chalcopyrite semiconductors still has room for improvement for the future generation solar cells. The energy band gaps of CuInGaS/CuInGaSe/CuInGaSSe can be tuned from 0.98 to 2.40 eV, providing a wider optical-response for photovoltaic applications. In addition, fullerene C_{60} has been shown to improve metal electrodes by alloying and high-temperature annealing [62–64]. The nonlinear optical characteristics can be derived from the unique three-dimensional microstructure, moving away from the local restriction or electron coupling in the fullerene. At the same time, fullerene material is quite cost-effective and abundant on the earth. The fullerene film can be deposited by an evaporating process.

In this work, the function of a multilayer structurehas been studied by photoluminescence spectroscopy, microscopy, and impedance spectroscopy. This experiments would implement a process for the fabrication of ultra-thin $CuIn_{1-x}Ga_xSe_2$ HTM to be a unique Cu-based inorganic HTM for solar cells. The perovskite solar cells with thinned $CuIn_{1-x}Ga_xSe_2$ HTM were fabricated using a $CH_3NH_3PbI_3$ active absorbing layer for renewable energy applications, suitable for the next generation thin-film solar cellsand also beneficial to environmental protection.

2. Materials and Methods

The FTO/glasssubstrate (Hartford Glass, TECA7-RL, IN, USA) was cleaned using acetone (Sigma-Aldrich, MO, USA), ethanol (Sigma-Aldrich, MO, USA), and de-ionizedwater, each for 10 min, and then dried in an oven. Mo film has good conductive properties and was deposited onthe substrate

by a radio-frequency (RF) magnetron sputtering system. It was extremely salient to ascertain optimal sputtering conditions for Mo film because good adherence and low resistivity were necessary to ensure a high efficiency for solar cells. In order to ameliorate conventional architecture to develop a novel solar cell device structure, a thinner Mo material was the second back metal-electrode contact layer. The FTO material was the first layer of the back contactelectrode. Thus, the FTO also worked as an adhesion layer in the multilayer-structure of solar cells. Using a transparent conductive oxide film, such as FTO, leads to recombination to substantially lower the absorption at the Mo back metal-electrode contact layer, enhancing the efficiency for multi-junction solar cells. In this study, an RF sputtering system with a different power in conjunction with a different working Ar flow pressure was explored to prepare bi-layer Mo films. The bi-layer Mo films obtained at a low sputtering pressure experienced compressive stress, which displayed low electrical resistivity but adhered poorly to the substrate. On the other hand, the bi-layer Mo films using high-pressure deposition could experience tensile stress and would adhere well to the substrate but displayed high electrical resistivity. The deposition was thus modified to include a porous bottom layer and a dense top layer. The combination of a higher working pressure and a lower working pressure has been attempted. In this experiment, the bottom layer was deposited at a higher Ar flow pressure and the Ar flow rate and RF power were maintained at 80 sccm and 120 W. Additionally, the top layer was deposited at a lower Ar flow pressure condition and the Ar flow rate and RF power were maintained at 40 sccm and 60 W for better adhesion and to ensure a low resistivity. Each Mo film with an approximate thickness of 100 nm was deposited. The Mo appeared as an excellent choice for the back metal-contact material as a result of its relative stability at the annealing temperature, better ohmic-contact for alloying with copper and indium, and its low contact resistance to the $CuIn_{1-x}Ga_xSe_2$ solar cells. The Mo film also acted as a reflective layer in the $CuIn_{1-x}Ga_xSe_2$ solar cells. The $CuIn_{1-x}Ga_xSe_2$ HTM films adjacent to the back-contact layer can also enhance the role of the back metal-electrode contact material as an optical reflector.

The $CuIn_{1-x}Ga_xSe_2$ film was further deposited by an RF magnetron system using a $CuIn_{1-x}Ga_xSe_2$ target on the bi-layer Mo/FTO glass substrates. The argon flow rate and RF power were maintained at 60 sccm and 80 W, respectively. The $CuIn_{1-x}Ga_xSe_2$ film was sputtered on bi-layer Mo metal-electrode films as a hole-transport material layer. For ultra-thin $CuIn_{1-x}Ga_xSe_2$ HTM (<400 nm), a surface roughness effect transforms the optical absorbing thickness, which provides shunt paths between the back-electrode and the front-electrode through the optical-conductive buffer layer. At the CIGSe-Mo interface, the diffusion of Se could escalate the structural quality of the $CuIn_{1-x}Ga_xSe_2$ solar cells, the adherence of $CuIn_{1-x}Ga_xSe_2$/Mo metal-contact and the electrical contact at $CuIn_{1-x}Ga_xSe_2$/Mo metal-contact interface.

A thinner Mo film between FTO and $CuIn_{1-x}Ga_xSe_2$ HTM could improve the recombination ofpairsof electron-holes at the interface. This phenomenon of recombination provided a means of gaining access to ultra-thin $CuIn_{1-x}Ga_xSe_2$ HTM comparablewith the traditional bulk carrier of $CuIn_{1-x}Ga_xSe_2$ solar cells. $CuIn_{1-x}Ga_xSe_2$ HTM film with a thickness of 100–300 nm was deposited. The films were further treated by thermal annealing at 400, 500, or 600 °C in a tube furnace for 60 min in order to get exceptional crystallization. The solution-processed $MAPbI_3$ material was coated on a $CuIn_{1-x}Ga_xSe_2$ film and fabricated as an inverted perovskite solar cell. PbI_2 and MAI were dissolved in 1 mL of a co-solvent, involving dimethyl sulfoxide and γ-butyrolactone (volume ratio = 1:1), to form a perovskite precursor solution. The precursor solution was spin-coated on the $CuIn_{1-x}Ga_xSe_2$ at 1000 rpm and 5000 rpm for 10 s and 20 s, respectively, in a glove chamber filled withhigh purity nitrogen (>99.99%). The wet spin-coating of the $MAPbI_3$ thin-film was processed by dropping 50 μL of anhydrous toluene at 17 s. It was then annealed at 100 °C for 10 min. The perovskite film had a thickness of approximately 600 nm. Additionally, C_{60} is an n-type semiconductor material and the function is an electronic transport buffer layer in this photovoltaic multilayer nano-structure. This fullerene powder was prepared on a molybdenum metal-boat using a vacuum evaporation system. The C_{60} film with a thickness of 50 nm was deposited on the $MAPbI_3$ film. The fullerene was

designated as an electron-transporting buffer layer. It could bond with the upper silver metal-electrode contact layer while conducting the necessary photo-current through the neighboring layers.

Finally, the top silver metal-electrode contact film layer was deposited with athickness of 100 nm by athermal vacuum evaporator system (PSE-1.5KVA). This solar cell device was shadowed with a finger mask to define an active area of 0.5 × 0.2 cm^2 during the front silver metal-electrode material deposition. Figure 1 shows the complete device schematic diagram of the $MAPbI_3$ perovskite solar cells with an ultra-thin $CuIn_{1-x}Ga_xSe_2$ HTM layer. The crystallization results of the nano-structures of the thin-film solar cells were analyzed by a PANalyticalX'Pert Pro DY2840 X-ray diffraction (XRD) system with Cu Kα radiation (λ = 0.154nm). A field-emission scanning electron microscope system (Zeiss Gemini SEM) was applied to take regard of the nano-crystal surface pattern of the thin-film devices. The photoluminescence (PL) was estimated using a fluorescence spectrophotometer (Hitachi F-7000). The solar cell materials were alsocharacterized by micro-Raman spectroscopy (Horiba/Jon YvonLabRAM HR800). The current-density voltage (J–V) characteristics of the devices were measured using a Keithley 2420 programmable source meter system under irradiation from a 1000 W xenon lamp. The measurement forward scan rate was 0.1 V/s. The irradiation power density on the surface of the sample was calibrated to 1000 W/m^2.

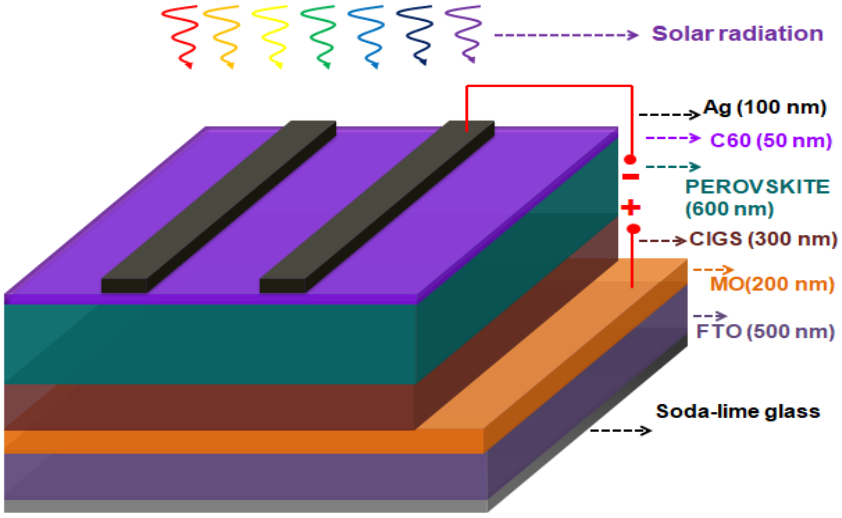

Figure 1. A schematic diagram of the perovskite solar cell with ultra-thin $CuIn_{1-x}Ga_xSe_2$ hole-transporting material layer.

3. Results and Discussion

The morphology of the $CuIn_{1-x}Ga_xSe_2$ HTM film was investigated by SEM. Figure 2 showsthe top-view SEM morphology ofthe $CuIn_{1-x}Ga_xSe_2$ HTM films following thermal annealing at various temperatures. The as-formed $CuIn_{1-x}Ga_xSe_2$ HTM films exhibited full surface coverage and were composed of crystal grains ranging from tens of nm to one μm in size. It has also been evidenced that the nano-crystal grain size increased following the higher annealing temperature. A densely crystallized $CuIn_{1-x}Ga_xSe_2$ HTM film could be acquired after sintering at the annealing temperature. However, the $CuIn_{1-x}Ga_xSe_2$ HTM film surface appearance at 400 °C, in Figure 2a, exhibited relatively smaller crystal grains from tens to 300 nm, also involving more pinholes. This defect phenomenon could facilitate incomplete bonding between the multilayer films. Figure 2b showsthe $CuIn_{1-x}Ga_xSe_2$ HTM film surface appearance from 500 °C annealing with crystallization from tens to 600 nm in grain size, involving fewer pinholes at the same resolution. Figure 2c shows the $CuIn_{1-x}Ga_xSe_2$ HTM film surface annealed at 600 °C. It exhibited crystals from tens nm to 1 μm in grain size, with scarce pinholes at the same resolution. The lower annealing temperature, on this occasion, led to a film surface involved in more defects or pinholes.

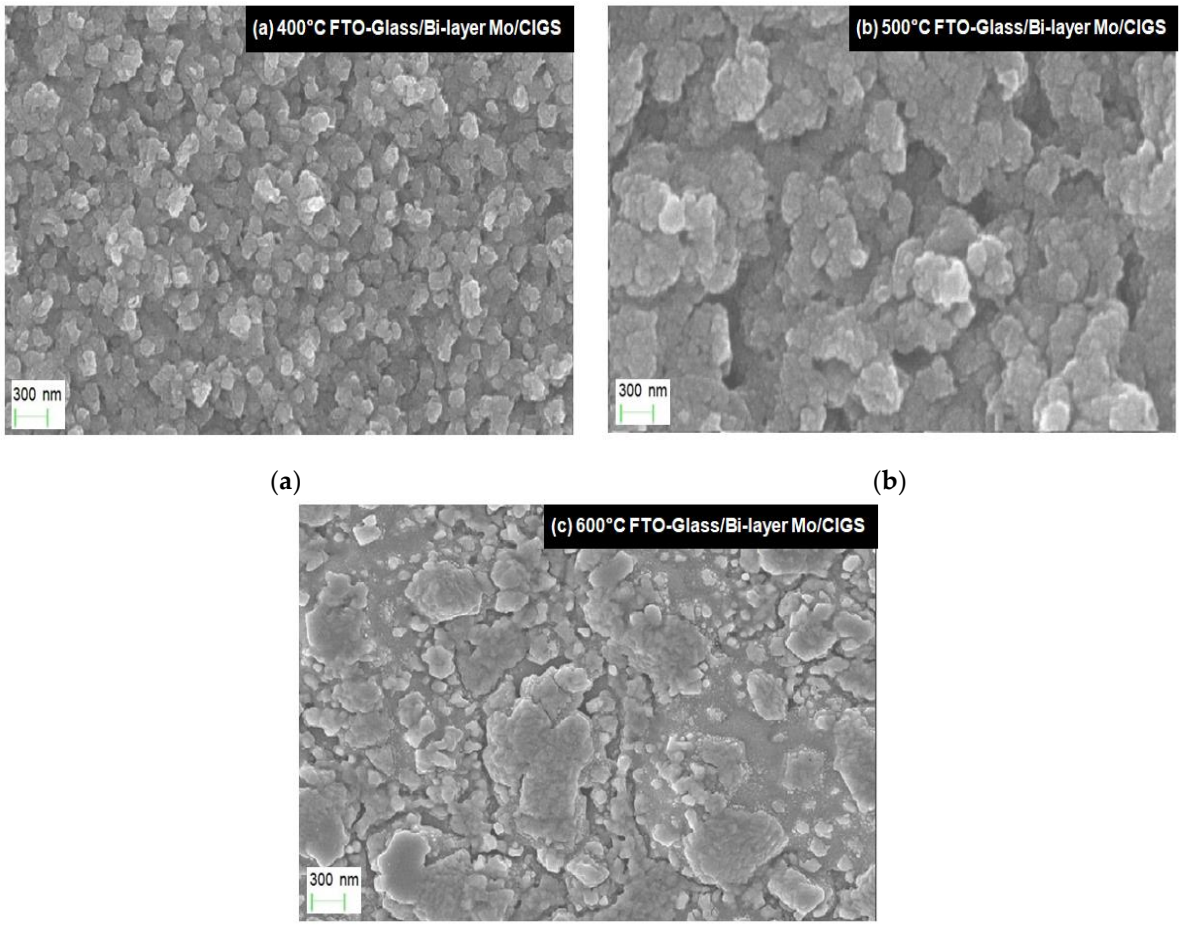

Figure 2. Top-view scanning electron microscope images of the ultra-thin $CuIn_{1-x}Ga_xSe_2$ hole-transporting material layer following thermal annealing at the various temperatures (**a**) 400 °C, (**b**) 500 °C, and (**c**) 600 °C.

Figure 3 displays the X-ray diffraction spectra of the multi-layer structures. The $MAPbI_3$ film's nano-crystals exhibit one main crystal plane (110) corresponding to the diffraction peak at ∼14.3°, indicating a strong preferential orientation in the growth direction. The other $MAPbI_3$ film's crystal plane (220) corresponds to the diffraction peak at ∼29.2°, and crystal plane (310) corresponds to the diffraction peak at ∼32.4°. On the other hand, the $CuIn_{1-x}Ga_xSe_2$ HTM film nano-crystals exhibit one main crystal plane (112) diffraction peak at ∼26.8°, indicating a strong preferential orientation in the growth direction. It also shows crystal planes (204) (220) diffraction peak at ∼44.9°, and crystal planes (312) (316) diffraction peak at ∼53.0°. The bi-layer Mo film's nano-crystals exhibit one main crystal plane (110) diffraction peak at ∼40.5°. Other bi-layer Mo film nano-crystals include a crystal plane (200) diffraction peak at ∼58.6° and a crystal plane (211) diffraction peak at ∼73.5°. Additionally, the $MoSe_2$ film nano-crystals exhibit one main crystal plane (011) diffraction peak at ∼13.5°, and crystal planes (224) (314) diffraction peak at ∼36.5°, and crystal plane (002) diffraction peak at ∼57°. The crystallization of $MAPbI_3$ active absorber layer was preceded by the ascension annealing temperature of the $CuIn_{1-x}Ga_xSe_2$ HTM film. The function of the $CuIn_{1-x}Ga_xSe_2$ HTM film was a hole-transporting layer and the function of $MAPbI_3$was as an active photovoltaic layer. In addition, the $CuIn_{1-x}Ga_xSe_2$ HTM film and the $MAPbI_3$ film could be sintered together. Furthermore, the $MAPbI_3$ and $CuIn_{1-x}Ga_xSe_2$ HTM films' energy band gapscan be complementary for trapping light simultaneously. As a result, it is composed of pairs of an excited electron and an associated

electron-hole for recombination. Subsequently, it can escalate the photon-electron power-conversion efficiency and the associated optical-current for the multilayer structure cells.

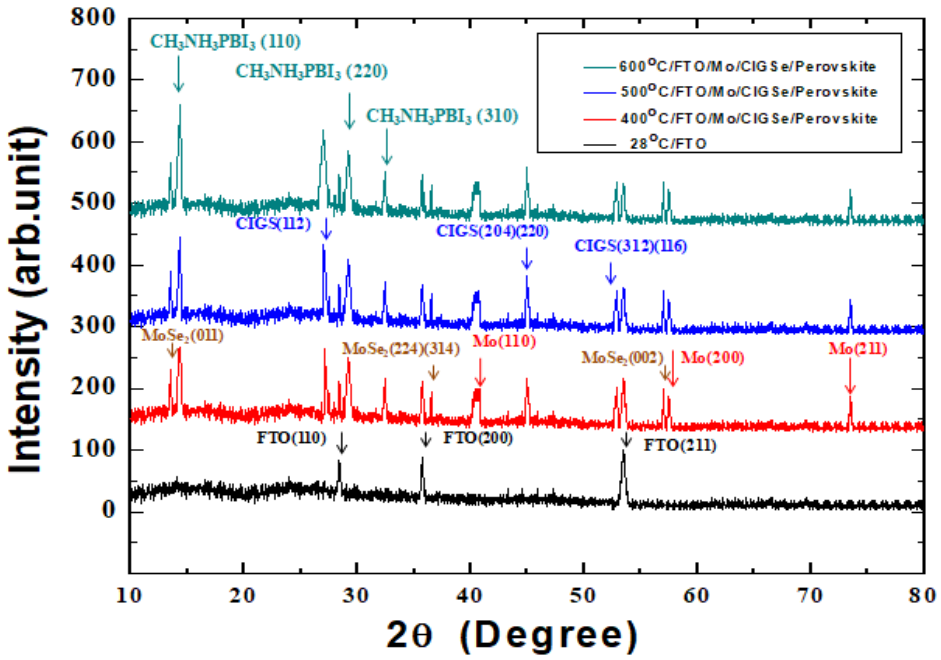

Figure 3. The X-ray diffraction pattern results of $CH_3NH_3PbI_3$ ($MAPbI_3$) perovskite solar cells with $CuIn_{1-x}Ga_xSe_2$ HTM (hole-transporting material) multi-layer structures.

Figure 4 shows the photoluminescence (PL) spectra of the $MAPbI_3$/CIGSe/bi-layer Mo/FTO glass following thermal annealing at the various temperatures. One main peak of the PL spectrum wavelength at ~767 nm is observed. The PL spectrum is light emission from any form of matter after the absorption of photons or electromagnetic radiation. The intensity is associated with the lifetime of the injected electrons and holes that were combined to form excitons in the solar cells. The excitons revealed mobile concentration energy formation by an excited electron and an associated electron-hole. As the excitons intensified during the examination, the number of excitons was enhanced and the electron/electron-hole recombined with each other. As the annealing temperature was increased from 400 to 600 °C, the PL intensity of the $MAPbI_3$ film deposited on the $CuIn_{1-x}Ga_xSe_2$ HTM film was enhanced. The $MAPbI_3/CuIn_{1-x}Ga_xSe_2$ HTM nano-crystals grown by annealing resulted in ohmic-contact construction and low contact resistance of the $CuIn_{1-x}Ga_xSe_2$ HTM film with bi-layer Mo film. The $CuIn_{1-x}Ga_xSe_2$ HTM film was conceived to havegood contact with the active $MAPbI_3$ absorbing layer in the solar cells to improve device stability.

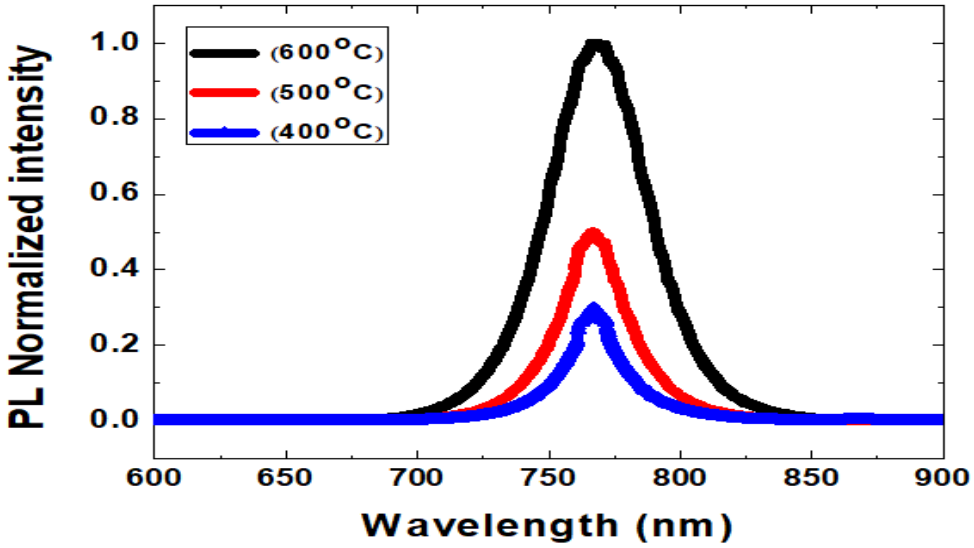

Figure 4. PL (photoluminescence) spectra of $MAPbI_3$/CIGSe HTM/bi-layerMo/FTO (fluorine-tin-oxide) glass following various thermal annealing temperatures at 400, 500, and 600 °C.

Figure 5 shows the SEM cross-sectional view of the $MAPbI_3$ on CIGSe HTM/bi-layer Mo/FTO glass multi-layer structure, with annealing at 600 °C. The solar cells have been composed of a relatively smooth CIGSe surface, involving few pinholes. Nevertheless, a complete solar cell multi-layer structure of $Ag/C_{60}/MAPbI_3/CIGSe/Mo/FTO$ was clearly revealed with a densely packed columnar architecture. Hereafter, Figure 6 shows a Tauc plot for measuring the energy band gap (E_g) at 1.25 eV for the $CuIn_{1-x}Ga_xSe_2$ HTM grown on a bi-layer Mo/FTO glass-substrate. The band-gap was obtained by extrapolating the linear portion of $(\alpha h\nu)^2$ vs. $h\nu$ graph, where α, h and ν represent the absorption, Planck constant and radiation frequency [65,66]. The energy band gap is required to elevate a valence electron bound to an atom to become a conduction electron and a hole, which can be free to move as charge carriers to conduct an electrical current.

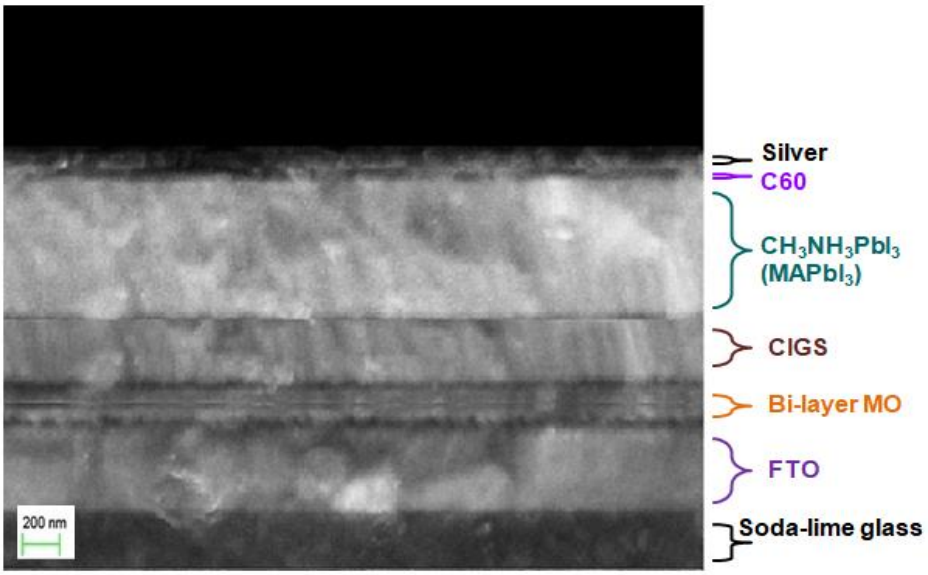

Figure 5. The field-emission SEM cross-sectional view of $CH_3NH_3PbI_3$ ($MAPbI_3$) the perovskite solar cell witha $CuIn_{1-x}Ga_xSe_2$ HTM/bi-layer Mo/FTO glass substrate. The $CuIn_{1-x}Ga_xSe_2$HTM layer was annealed at 600 °C.

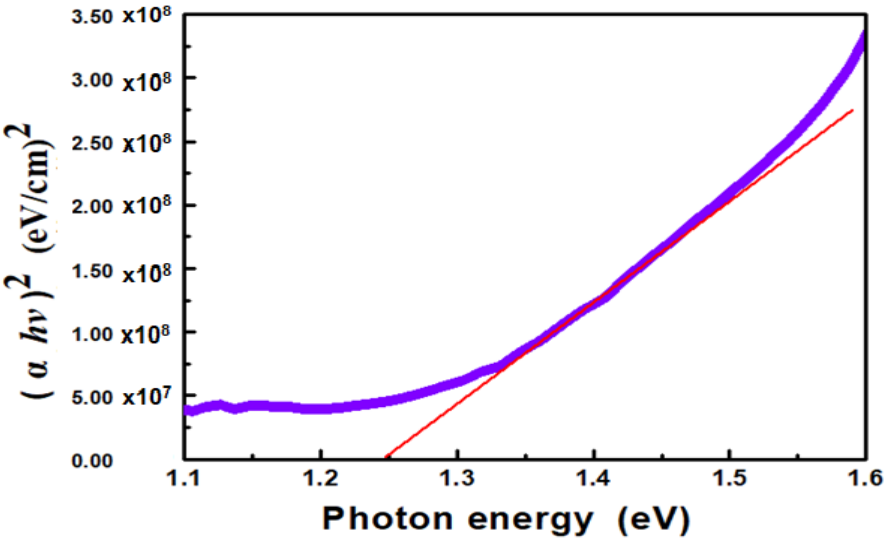

Figure 6. Tauc plot for measuring the energy band gap for $CuIn_{1-x}Ga_xSe_2$ HTM grown on a bi-layer Mo/FTO glass substrate. The red line was used to extrapolate the band-gap.

Figure 7 shows the plotted current-density voltage (J–V) curves of $MAPbI_3$ perovskite solar cells with the ultra-thin $CuIn_{1-x}Ga_xSe_2$HTM nano-structures on bi-layer Mo/FTO glass substrates. The various HTM thicknesses, all at an annealing temperature of 600 °C, were compared here under 100 mW/cm^2 illumination (AM 1.5G). At least six cell samples of each type have been fabricated, with the performance deviation ~5%. Additionally, Table 1 summarizes the characteristic parameters of the novel solar cells at the various HTM thicknesses using a 600 °C annealing temperature. The solar cells' open-circuit voltage could be increased from 0.96 to 1.02 V, with the $CuIn_{1-x}Ga_xSe_2$ HTM film from 100 to 300 nm. The short-circuit current value also increased from 20.4 to 20.9 mA/cm^2. The device fill factor values were slightly diminished from 67.4% to 65.6%. The photovoltaic device PCE ranged from 13.2% to 14.2%. In addition, the device series-resistance was decreased from 16.9 to 15.8 Ω. The output power Pmax effect values increased from 1.32 mW to 1.42 mW.

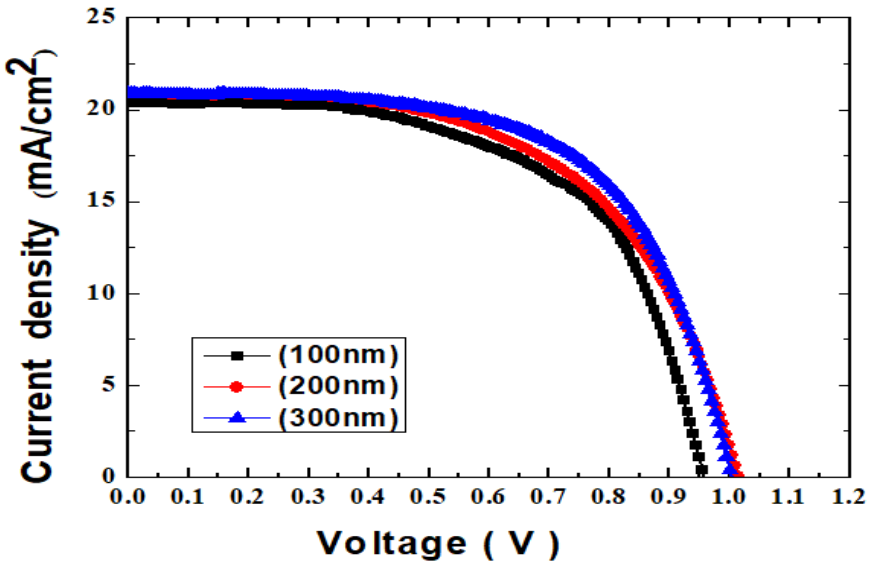

Figure 7. J–V curves of $MAPbI_3$ perovskite solar cells with ultra-thin $CuIn_{1-x}Ga_xSe_2$HTM nano-structures on a bi-layer Mo/FTO glass substrate, using various HTM thicknesses with a 600 °C thermal annealing temperature. Measurement under 100 mW/cm^2 illumination (AM 1.5G).

Table 1. Characteristic parameters of the novel solar cells at the various HTM thicknesses using a 600 °C thermal annealing temperature.

HTM Thickness (nm)	V_{OC} (V)	J_{SC} (mA/cm^2)	FF (%)	Eff (%)	R_S (Ω)	P_{max} (mW)
100	0.96	20.4	67.4	13.2	16.9	1.32
200	1.02	20.9	66.6	14.2	15.8	1.42
300	1.00	20.9	65.6	13.7	16.2	1.37

Furthermore, the fill factor has been defined as the ratio of the output power Pmax to the device open-circuit voltage and short-circuit current at the maximum electric power output. This is the maximum power of the rectangle in the current-voltage characteristic curve. In accordance with the current-density voltage curve and the PCE value, it has been suggested that the optimal thickness of the $CuIn_{1-x}Ga_xSe_2$ hole-transporting film layer is at ~200 nm. This sample exhibited a slightly higher open-circuit voltage along with the lowest device series-resistance. In this study, it has been desired to develop ultra-thin HTM layers for solar cell applications. The CIGS film quality has been improved and the HTM layer thickness was decreased. In fact, the 300 nm sample also exhibited a reasonably good PSC performance. On the other hand, when the CIGS layer was tried at a thickness below 100 nm (such as 30–50 nm, not shown in this report), not only was the PSC performance was degraded but also the deviation increased appreciably.

An ultra-thin $CuIn_{1-x}Ga_xSe_2$HTM (<400 nm) has been deposited between the $MAPbI_3$ active absorber material and the bi-layer Mo metal-electrode to promote carrier transport, leading to an improved device witha goodohmic-contact. Additionally, innovative structures of bi-layer Mo films were deposited onto FTO/glass substrates. Eventually, Figure 8 shows the ultra-thin $CuIn_{1-x}Ga_xSe_2$ hole-transporting material detailed investigation on the compositional dependence of the Raman spectra, grown on a bi-layer Mo/FTO glass substrate. In this work, the $CuIn_{1-x}Ga_xSe_2$ HTM film exhibited dominant spectra with an intense Raman scattering peak at 174 cm^{-1}, corresponding to the optical phonon mode that was characteristic of the chalcopyrite nano-crystals and nano-structures. The Raman intensities at 174 cm^{-1}, 214 cm^{-1} and 240 cm^{-1} were slightly increased while increasing the annealing temperature. The $CuIn_{1-x}Ga_xSe_2$ HTM crystal orientation could be found from the polarization of Raman-scattered light with respect to the laser light if the crystal structure's point group was known.

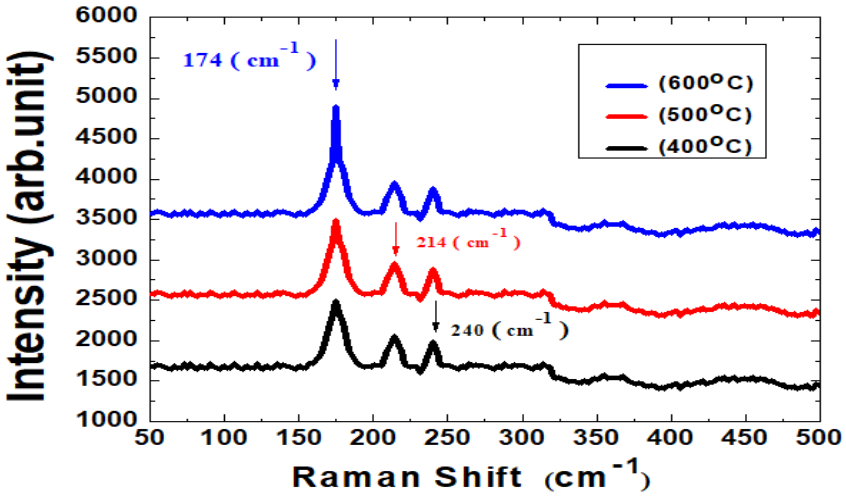

Figure 8. Compositional dependence of Raman spectra of $CuIn_{1-x}Ga_xSe_2$ hole-transporting material layer that was grown on a bi-layer Mo/FTO glass substrate.

Figure 9 shows the device measured external quantum efficiency (EQE) curve results due to optical modification with $CuIn_{1-x}Ga_xSe_2$ hole-transporting material. The spectra included experimentally

measured EQE curves with an entire major spectral feature, which reproduced in both wavelength and amplitude. Notably, the EQE results with ultra-thin $CuIn_{1-x}Ga_xSe_2$ HTM exhibited the maximum EQE of ~78% for the 600 °C-annealed sample, observed between 500 nm and 600 nm. It was attributed to the combined effects of Fabry-Perot resonances and efficient coupling into the waveguide modes of the absorber layer [67,68]. Planar $CuIn_{1-x}Ga_xSe_2$ solar cells contained translational invariant and an electric field distribution by resonances.

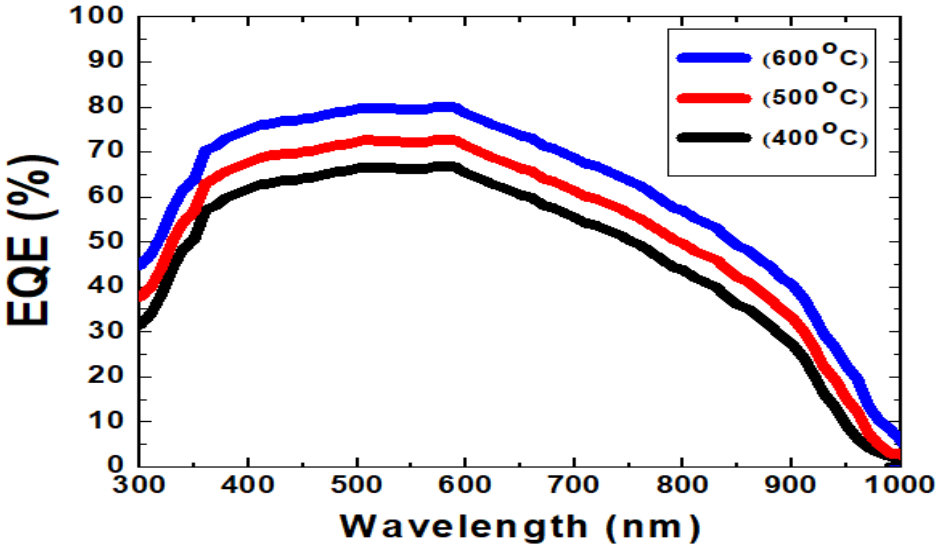

Figure 9. The measured results of external quantum efficiency (EQE) spectra based onsilver/C_{60}/$MAPbI_3$/CIGSe/Mo/FTO solar cells.

4. Conclusions

In summary, sputtering-processed $CuIn_{1-x}Ga_xSe_2$ nano-crystals have been successfully applied as a novel Cu-based inorganic HTM for solar cells. The PCE of the $CuIn_{1-x}Ga_xSe_2$ HTM-based photovoltaic device has been reached at 14.2%, which is quite encouraging for conventional solar cells with Cu-based chalcopyrite semiconductor HTMs. In addition, the $CuIn_{1-x}Ga_xSe_2$ HTM/$MAPbI_3$ perovskite layers that involved $MoSe_2$ exhibited a good ohmic-contact. This work provided a promising candidate of Cu-based inorganic HTM for stable perovskite solar cells, and dedicated investigation about characteristics of silver/C_{60}/$CH_3NH_3PbI_3$/CIGSe/bi-layer Mo/FTO multilayer of nano-structured devices. The SEM morphology observation on $CuIn_{1-x}Ga_xSe_2$ HTM film following thermal annealing at 400, 500, and 600 °C revealed crystal grains ranging from tens nm to one μm in size. The pinhole and defect density wasalso decreased with the increasing annealing temperature. The experimental results of $MAPbI_3$ perovskite solar cells with the optimal 200 nm $CuIn_{1-x}Ga_xSe_2$ HTM nano-structures that were annealed at 600 °C showed a better PCE of 14.2%. This device exhibited that the V_{OC}, J_{SC}, FF, PCE, Rs, and Pmax were 1.02 V, 20.9 mA/cm^2, 66.6%, 14.2%, 15.8 Ω, and 1.42 mW, respectively.

Author Contributions: Investigation, L.-B.C., C.-C.T., G.W., W.-S.F. and M.-J.J.; methodology, L.-C.C. and K.-L.L.; resources, E.P., L.J. and K.G.; writing—original draft preparation, C.-C.T.; writing—review and editing, G.W.

Funding: This work was supported in part by the Ministry of Science and Technology under research grants MOST105-2221-E182-059-MY3, MOST105-2221-B182-059-MY3, and MOST106-2221-E182-060. The APC was funded by CGMH/CGU under CMRPD3G0062 and BMRP246.

Conflicts of Interest: The authors declare no conflict of interest.

References

1. Correa-Baena, J.B.; Abate, A.; Saliba, M.; Tress, W.; Jacobsson, T.J.; Gratzelc, M.; Hagfeldt, A. The rapid evolution of highly efficient perovskite solar cells. *Energy Environ. Sci.* **2017**, *10*, 710–727. [CrossRef]
2. Dubey, A.; Adhikari, N.; Mabrouk, S.; Wu, F.; Chen, K.; Yang, S.; Qiao, Q. A strategic review on processing routes towards highly efficient perovskite solar cells. *J. Mater. Chem. A* **2018**, *6*, 2406–2431. [CrossRef]
3. Meng, L.; You, J.; Guo, T.; Yang, Y. Recent advances in the inverted planar structure of perovskite solar cells. *Acc. Chem. Res.* **2016**, *49*, 155–165. [CrossRef]
4. Dubey, A.; Adhikari, N.; Venkatesan, S.; Gu, S.; Khatiwada, D.; Wang, Q.; Mohammad, L.; Kumar, M.; Qiao, Q. Solution processed pristine PDPP3T polymer as hole-transport layer for efficient perovskite solar cells with slower degradation. *Solar Energy Mater. Solar Cells* **2016**, *145*, 193–199. [CrossRef]
5. Wu, W.; Chen, D.; Caruso, R.A.; Cheng, Y. Recent progress in hybrid perovskite solar cells based on n-type materials. *J. Mater. Chem. A* **2017**, *5*, 10092–10109. [CrossRef]
6. Ahmadian-Yazdi, M.; Habibi, M.; Esiamian, M. Excitation of wet perovskite films by ultrasonic vibration improves the device performance. *Appl. Sci.* **2018**, *8*, 308. [CrossRef]
7. Zuo, C.; Bolink, H.J.; Han, H.; Huang, J.; Cahen, D.; Ding, L. Advances in perovskite solar cells. *Adv. Sci.* **2016**, *3*, 1500324. [CrossRef]
8. Wang, R.; Wu, X.; Xu, K.; Zhou, W.; Shang, Y.; Tang, H.; Chen, H.; Ning, Z. Highly efficient inverted structural quantum dot solar cells. *Adv. Mater.* **2018**, *30*, 1704882. [CrossRef]
9. Pierini, F.; Lanzi, M.; Nakielski, P.; Pawlowska, S.; Urbanek, O.; Zembrzycki, K.; Kowalewski, T.A. Single-material organic solar cells based on electro spun fullerene-grafted polythiophene nanofibers. *Macromolecules* **2017**, *50*, 4972–4981. [CrossRef]
10. Mitzi, D.B.; Chondroudis, K.; Kagan., C.R. Design, structure, and optical properties of organic inorganic perovskites containing an oligothiophenechromophor. *Prog. Inorg. Chem.* **1999**, *38*, 6246–6256. [CrossRef]
11. Mitzi, D.B. Synthesis, structure, properties of organic-inorganic perovskites and related materials. *Prog. Inorg. Chem.* **2007**, *48*, 1–121.
12. Jeon, N.J.; Noh, J.H.; Yang, W.S.; Kim, Y.C.; Ryu, S.; Seo, J.; Seok, S.I. Compositional engineering of perovskite materials for high-performance solar cells. *Nature* **2015**, *517*, 476. [CrossRef] [PubMed]
13. Liu, M.; Johnston, M.B.; Snaith, H.J. Efficient planar heterojunction perovskite solar cells by vapour deposition. *Nature* **2013**, *501*, 396. [CrossRef] [PubMed]
14. Im, J.H.; Jang, I.H.; Pellet, N.; Gratzel, M.; Park, N. Growth of $CH_3NH_3PbI_3$ cuboids with controlled size for high-efficiency perovskite solar cells. *Nat. Nanotechnol.* **2014**, *9*, 927–932. [CrossRef] [PubMed]
15. Yang, W.S.; Noh, J.H.; Jeon, N.J.; Kim, Y.C.; Ryu, S.; Seo, J.; Seok, S.I. High-performance photovoltaic perovskite layers fabricated through intramolecular exchange. *Science* **2015**, *348*, 1234–1237. [CrossRef] [PubMed]
16. Sani, F.; Shafie, S.; Lim, H.N.; Musa, A.O. Advancement on lead-free organic-inorganic halide perovskite solar cells: A review. *Materials* **2018**, *11*, 1008. [CrossRef]
17. Xing, G.; Mathews, N.; Sun, S.; Lim, S.S.; Lam, Y.M.; Gratzel, M.; Mhaisalkar, S.; Sum, T.C. Long-range balanced electron- and hole-transport lengths in organic-inorganic $CH_3NH_3PbI_3$. *Science* **2013**, *342*, 344–347. [CrossRef]
18. Stranks, S.D.; Eperon, G.E.; Grancini, G.; Menelaou, C.; Alcocer, M.J.; Leijtens, T.; Herz, L.M.; Petrozza, A.; Snaith, H.J. Electron-hole diffusion lengths exceeding 1 micrometer in an organometaltrihalide perovskite absorber. *Science* **2013**, *342*, 341–344. [CrossRef]
19. Kojima, A.; Teshima, K.; Shirai, Y.; Miyasaka, T. Organometal halide perovskites as visible-light sensitizers for photovoltaic cells. *J. Am. Chem. Soc.* **2009**, *131*, 6050–6051. [CrossRef]
20. Kim, H.S.; Lee, C.R.; Im, J.H.; Lee, K.B.; Moehl, T.; Marchioro, A.; Moon, S.J.; Humphry-Baker, R.; Yum, J.H.; Moser, J.E.; et al. Lead iodide perovskite sensitized all-solid-state submicron thin film mesoscopic solar cell with efficiency exceeding 9%. *Sci. Rep.* **2012**, *2*, 591. [CrossRef]
21. Jeng, J.Y.; Chiang, Y.F.; Lee, M.H.; Peng, S.R.; Guo, T.F.; Chen, P.; Wen, T.C. $CH_3NH_3PbI_3$ perovskite/fullerene planar-heterojunction hybrid solar cells. *Adv. Mater.* **2013**, *25*, 3727–3732. [CrossRef] [PubMed]
22. Chen, L.M.; Hong, Z.; Li, G.; Yang, Y. Recent progress in polymer solar cells: Manipulation of polymer: Fullerene morphology and the formation of efficient inverted polymer solar cells. *Adv. Mater.* **2009**, *21*, 1434–1449. [CrossRef]

23. Choi, H.; Mai, C.; Kim, H.; Jeong, J.; Song, S.; Bazan, G.C.; Kim, J.Y.; Heeger, A.J. Conjugated polyelectrolyte hole transport layer for inverted-type perovskite solar cells. *Nat. Commun.* **2015**, *6*, 7348. [CrossRef] [PubMed]
24. Li, Z.; Klein, T.R.; Kim, D.H.; Yang, M.; Berry, J.J.; van Hest, M.F.; Zhu, K. Scalable fabrication of perovskite solar cells. *Nat. Rev. Mater.* **2018**, *3*, 18017. [CrossRef]
25. Christians, J.A.; Schulz, P.; Tinkham, J.S.; Schloemer, T.H.; Harvey, S.P.; Tremolet de Villers, B.J.; Sellinger, A.; Berry, J.J.; Luther, J.M. Tailored interfaces of unencapsulated perovskite solar cells for >1000 hour operational stability. *Nat. Energy* **2018**, *3*, 68–74. [CrossRef]
26. Snaith, H.J.; Hacke, P. Enabling reliability assessments of pre-commercial perovskite photovoltaics with lessons learned from industrial standards. *Nat. Energy* **2018**, *3*, 459–465. [CrossRef]
27. Habisreutinger, S.N.; McMeekin, D.P.; Snaith, H.J.; Nicholas, R.J. Research update: Strategies for improving the stability of perovskite solar cells. *APL Mater.* **2016**, *4*, 091503. [CrossRef]
28. Kim, J.; Yang, J.; Yu, J.H.; Baek, W.; Lee, C.; Son, H.J.; Hyeon, T.; Ko, M.J. Highly efficient copper–indium–selenide quantum dot solar cells: Suppression of carrier recombination by controlled ZnS overlayers. *ACS Nano* **2015**, *9*, 11286–11295. [CrossRef]
29. Lian, L.; Xia, Y.; Zhang, C.; Xu, B.; Yang, L.; Liu, H.; Zhang, D.; Wang, K.; Gao, J.; Zhang, J. In situ tuning the reactivity of selenium precursor to synthesize wide range size, ultra large-scale, and ultrastable PbSe quantum dots. *Chem. Mater.* **2018**, *30*, 982–989. [CrossRef]
30. Wen, X.; Chen, C.; Lu, S.; Li, K.; Kondrotas, R.; Zhao, Y.; Chen, W.; Gao, L.; Wang, C.; Zhang, J.; et al. Vapor transport deposition of antimony selenide thin film solar cells with 7.6% efficiency. *Nat. Commun.* **2018**, *9*, 2179. [CrossRef]
31. Sapkota, Y.R.; Mazumdar, D. Bulk transport properties of bismuth selenide thin films grown by magnetron sputtering approaching the two-dimensional limit. *J. Appl. Phys.* **2018**, *124*, 105306. [CrossRef]
32. Wei, S.H.; Zunger, A. Band offsets and optical bowings of chalcopyrites and Zn-based II-VI alloys. *J. Appl. Phys.* **1995**, *78*, 3846–3856. [CrossRef]
33. Van Lare, C.; Yin, G.; Polman, A.; Schmid, M. Light coupling and trapping in ultrathin Cu(In,Ga)Se_2 solar cells using dielectric scattering patterns. *ACS Nano* **2015**, *9*, 9603–9613. [CrossRef] [PubMed]
34. Han, A.; Zhang, Y.; Song, W.; Li, B.; Liu, W.; Sun, Y. Structure, morphology and properties of thinned Cu(In, Ga)Se_2 films and solar cells. *Semicond. Sci. Technol.* **2012**, *27*, 3. [CrossRef]
35. Saifullah, M.; Ahn, S.; Gwak, J.; Ahn, S.; Kim, K.; Cho, J.; Park, J.H.; Eo, Y.J.; Cho, A.; Yoo, J.U.; et al. Development of semitransparent CIGS thin-film solar cells modified with a sulfurized-AgGa layer for building applications. *J. Mater. Chem. A* **2016**, *4*, 10542–10551. [CrossRef]
36. Wu, G.M.; Lin, H.H.; Lu, H.C. Work function and valance band structure of tin-doped indium oxide thin film for OLED. *Vacuum* **2008**, *82*, 1371. [CrossRef]
37. Yin, G.; Brackmann, V.; Hoffmann, V.; Schmid, M. Enhanced performance of ultra-thin Cu(In,Ga)Se_2 solar cells deposited at low process temperature. *Solar Energy Mater. Solar Cells* **2005**, *132*, 142–147. [CrossRef]
38. Martin, F.; Muralt, P.; Dubois, M.A. Process optimization for the sputter deposition of molybdenum thin films as electrode for AlN thin films. *J. Vacuum Sci. Technol. A* **2006**, *24*, 946–952. [CrossRef]
39. Li, Z.H.; Cho, E.S.; Kwon, S.J. Molybdenum thin film deposited by in-line DC magnetron sputtering as a back contact for Cu(In,Ga)Se_2 solar cells. *Appl. Surf. Sci.* **2011**, *257*, 9682–9688. [CrossRef]
40. Ma, X.; Liu, D.; Yang, L.; Zuo, S.; Zhou, M. Molybdenum (Mo) back contacts for CIGS solar cell. *Proc. of SPIE* **2013**, *9068*, 906814. [CrossRef]
41. Jaegaermann, W.; Loher, T.; Pettenkofer, C. Surface properties of chalcopyrite semiconductors. *Cryst. Res. Cryst. Technol.* **1996**, *31*, 273.
42. Alvarez-Garcia, J.; Perez-Rodriguez, A.; Romano-Rodriguez, A.; Morante, J.R.; Calvo-Barrio, L.; Scheer, R.; Klenk, R. Microstructure and secondary phases in co-evaporated CuInS2 films: Dependence on growth temperature and chemical composition. *J. Vac. Sci. Technol. A* **2001**, *19*, 232–239. [CrossRef]
43. Wada, T.; Kohara, N.; Nishiwaki, S.; Negami, T. Characterization of the Cu (In, Ga) Se_2/Mo interface in CIGS solar cells. *Thin Solid Films* **2001**, *387*, 118–122. [CrossRef]
44. Schmid, D.; Ruckh, M.; Schock, H.W. A comprehensive characterization of the interfaces in Mo/CIS/CdS/ZnOsolarcell structures. *Solar Energy Mater. Solar Cells* **1996**, *41*, 281–294. [CrossRef]

45. Klinkert, T.; Patriarche, G.; Theys, B.; Theys, B. New insights into the Mo/Cu(In,Ga)Se_2 interface in thin film solar cells: Formation and properties of the $MoSe_2$ interfacial layer. *J. Chem. Phys.* **2016**, *145*, 154702. [CrossRef] [PubMed]
46. Wada, T.; Kohara, N.; Negami, T.; Nishitani, M. Chemical and structural characterization of Cu(In, Ga)Se_2/Mo interface in Cu(In, Ga)Se_2 solar cells. *Jpn. J. Appl. Phys.* **1996**, *35*, L1253–L1256. [CrossRef]
47. Duchatelet, A.; Savidand, G.; Vannier, R.N.; Lincot, D. Optimization of $MoSe_2$ formation for Cu(In,Ga)Se_2-based solar cells by using thin superficial molybdenum oxide barrier layers. *Thin Solid Films* **2013**, *545*, 94–99. [CrossRef]
48. Zhang, X.; Kobayashi, M.; Yamada, A. Comparison of Ag(In,Ga)Se_2/Mo and Cu(In,Ga)Se_2/Mo interfaces in solar cells. *ACS Appl. Mater. Interfaces* **2017**, *9*, 16215–16220. [CrossRef]
49. Schmid, M.; Klenk, R.; Lux-Steiner, M.C.; Topic, M. Modeling plasmonic scattering combined with thin-film optics. *Nanotechnology* **2011**, *22*, 025204. [CrossRef]
50. Schmid, M.; Klaer, J.; Klenk, R.; Topic, M.J. Stability of plasmonicmetalnanoparticles integrated in the back contact of ultra-thin Cu(In,Ga)S_2 solar cells. *Thin Solid Films* **2013**, *527*, 308–313. [CrossRef]
51. Amin, N.; Chelvanathan, P.; Hossain, M.I.; Sopian, K. Numerical modelling of ultra thin Cu(In,Ga)Se_2 solar cells. *Energy Procedia* **2011**, *15*, 291–298. [CrossRef]
52. Gloeckler, M.; Sites, J.R. Potential of submicrometer thickness Cu(In,Ga)Se_2 solar cells. *J. Appl. Phys.* **2005**, *98*, 103703. [CrossRef]
53. Xu, L.; Deng, L.; Cao, J.; Wang, X.; Chen, W.; Jiang, Z. Solution-processed Cu(In,Ga)$(S,Se)_2$ nanocrystal as inorganic hole-transporting material for efficient and stable perovskite solar cells. *Nanoscale Res. Lett.* **2017**, *12*, 159. [CrossRef] [PubMed]
54. Heo, J.H.; Im, S.H.; Noh, J.H.; Mandal, T.N.; Lim, C.S.; Chang, J.A.; Lee, Y.H.; Sarkar, A.; Nazeeruddin, M.K. Efficient inorganic-organic hybrid heterojunction solar cells containing perovskite compound and polymeric hole conductors. *Nat. Photonic* **2013**, *7*, 486–491. [CrossRef]
55. Noh, J.H.; Im, S.H.; Heo, J.H.; Mandal, T.N.; Seok, S.I. Chemical management for colorful, efficient, and stable inorganic-organic hybrid nanostructured solar cells. *Nano. Lett.* **2013**, *13*, 1764–1769. [CrossRef] [PubMed]
56. Niu, G.; Li, W.; Meng, F.; Wang, L.; Dong, H.; Qiu, Y. Study on the stability of $CH_3NH_3PbI_3$ ($MAPbI_3$) films and the effect of post-modification by aluminum oxide in all-solid-state hybrid solar cells. *J. Mater. Chem. A* **2014**, *2*, 705–710. [CrossRef]
57. Christians, J.A.; Fung, R.C.; Kamat, P.V. An inorganic hole conductor for organo-lead halide perovskite solar cells: Improved hole conductivity with copper iodide. *J. Am. Chem. Soc.* **2013**, *136*, 758–764. [CrossRef]
58. Chen, W.Y.; Deng, L.L.; Dai, S.M.; Wang, X.; Tian, C.B.; Zhan, X.X.; Xie, S.Y.; Huang, R.B.; Zheng, L.S. Low-cost solution-processed copper iodide as an alternative to PEDOT:PSS hole transport layer for efficient and stable inverted planar heterojunction perovskite solar cells. *J. Mater. Chem. A* **2015**, *3*, 19353–19359. [CrossRef]
59. Li, Y.; Zhu, J.; Huang, Y.; Wei, J.; Liu, F.; Shao, Z.; Hu, L.; Chen, S.; Yang, S.; Tang, J.; et al. Efficient inorganic solid solar cells composed of perovskite and PbS quantum dots. *Nanoscale* **2015**, *7*, 9902–9907. [CrossRef]
60. Kim, J.H.; Liang, P.W.; Williams, S.T.; Cho, N.; Chueh, C.C.; Glaz, M.S.; Ginger, D.S.; Jen, A.K. High-performance and environmentally stable planar heterojunction perovskite solar cells based on a solution-processed copper-doped nickel oxide hole-transporting layer. *Adv. Mater.* **2015**, *27*, 695–701. [CrossRef]
61. Lu, M.; Zhu, J.; Huang, Y.; Li, Y.; Shao, Z.; Xu, Y.; Dai, S. Colloidal $CuInS_2$ quantum dots as inorganic hole-transporting material in perovskite solar cells. *ACS Appl. Mater. Interfaces* **2015**, *7*, 17482–17488.
62. Chen, J.; Park, N. Inorganic hole transporting materials for stable and high efficiency perovskite solar cells. *J. Phys. Chem. C* **2018**, *8*, 01177. [CrossRef]
63. Yoshida, K.; Oku, T.; Suzuki, A.; Akiyama, T.; Yamasaki, Y. Fabrication and characterization of phthalocyanine/C_{60} solar cells with inverted structure. *Adv. Chem. Eng. Sci.* **2012**, *2*, 461–464. [CrossRef]
64. Kim, D.Y.; So, F.; Gao, Y. Aluminum phthalocyanine chloride/C_{60} organic photovoltaic cells with high open-circuit voltages. *Solar Energy Mater. Solar Cells* **2009**, *93*, 1688–1691. [CrossRef]
65. Bakr, N.A.; Khodair, Z.T.; Mahdi, H.I. Influence of thiourea concentration on some physical properties of chemically sprayed Cu_2ZnSnS_4 thin films. *Intl. J. Mater. Sci. Appl.* **2016**, *5*, 261–270.
66. Sahoo, A.K.; Wu, G.M. Effects of argon flow rate on electrical properties of amorphous indium gallium zinc oxide thin-film transistors. *Thin Solid Films* **2016**, *605*, 129–135. [CrossRef]

67. Yin, G.; Knight, M.W.; van Lare, M.; Magdalena, M.; Garcia, S.; Polman, A.; Schmid, M. Optoelectronic enhancement of ultrathin $CuIn_{1-x}Ga_xSe_2$solar cells by nanophotonic contacts. *Adv. Opt. Mater.* **2017**, *5*, 1600637. [CrossRef]
68. Jheng, B.T.; Liu, P.; Wu, M. Efficiency enhancement of non-selenized $Cu(In,Ga)Se_2$ solar cells employing scalable low-cost antireflective coating. *Nanoscale Res. Lett.* **2014**, *9*, 331. [CrossRef]